The Astrophysical Journal, 791:26 (9pp), 2014 August 10 doi:10.1088/0004-637X/791/1/26

ION PRE-ACCELERATION IN FULLY SELF-CONSISTENT PARTICLE-IN-CELL SIMULATIONS OF SUPERCRITICAL PERPENDICULAR REFORMING SHOCKS IN MULTIPLE ION SPECIES PLASMAS

V. L. Rekaa[1], S. C. Chapman[2,3,4], and R. O. Dendy[5,2]
[1] Department of Physics, University of Oslo, P.O. Box 1048 Blindern, N-0316 Oslo, Norway; v.l.rekaa@fys.uio.no
[2] CFSA, Department of Physics, University of Warwick, Coventry CV4 7AL, UK
[3] MPI-PKS, Nöthnitzer Str. 38, D-01187 Dresden, Germany
[4] Department of Mathematics and Statistics, University of Tromsø, P.O. Box 6050 Langnes, N-9037 Tromsø, Norway
[5] CCFE, Culham Science Centre, Abingdon, Oxfordshire OX14 3DB, UK
Received 2014 March 5; accepted 2014 June 2; published 2014 July 23

ABSTRACT

Supernova remnant and heliopause termination shock plasmas may contain significant populations of minority heavy ions, with relative number densities n_α/n_i up to 50%. Preliminary kinetic simulations of collisionless shocks in these environments showed that the reformation cycle and acceleration mechanisms at quasi-perpendicular shocks can depend on the value of n_α/n_i. Shock reformation unfolds on ion spatio-temporal scales, requiring fully kinetic simulations of particle dynamics, together with the self-consistent electric and magnetic fields. This paper presents the first set of particle-in-cell simulations for two ion species, protons (n_p) and α-particles (n_α), with differing mass and charge-to-mass ratios, that spans the entire range of n_α/n_i from 0% to 100%. The interplay between the differing gyro length scales and timescales of the ion species is crucial to the time-evolving phenomenology of the shocks, the downstream turbulence, and the particle acceleration at different n_α/n_i. We show how the overall energization changes with n_α/n_i, and relate this to the processes individual ions undergo in the shock region and in the downstream turbulence, and to the power spectra of magnetic field fluctuations. The crossover between shocks dominated by the respective ion species happens when $n_\alpha/n_i = 25\%$, and minority ion energization is strongest in this regime. Energization of the majority ion species scales with injection energy. The power spectrum of the downstream turbulence includes peaks at sequential ion cyclotron harmonics, suggestive of ion ring-beam collective instability.

Key words: acceleration of particles – cosmic rays – ISM: supernova remnants – methods: numerical – plasmas – shock waves

Online-only material: color figures

1. INTRODUCTION

Identification of the mechanisms by which particles are accelerated to cosmic ray energies in supernova remnants (SNRs) and at the heliopause termination shock (HTS) is an outstanding problem in astrophysics. While diffusive shock acceleration (Fermi 1949; Bell 1978; Blandford & Ostriker 1978) offers a potentially efficient process for the acceleration of particles that are already mildly relativistic, the "injection" problem remains: what physical processes pre-accelerate ambient background ions and electrons from low energies to mildly relativistic energies, at which stage diffusive shock acceleration can take over? Resolving this question requires careful analysis of plasma astrophysical kinetic processes (Kirk & Dendy 2001) in astrophysical shock environments through theory and direct numerical simulation. These efforts (e.g., Dieckmann et al. 2006; McClements et al. 2001) complement indirect and direct observations of particles in SNRs and at the HTS (Koyama et al. 1995; Enomoto et al. 2002), which show energy spectra, suggesting that perpendicular shocks are sites at which pre-acceleration mechanisms operate.

Recent particle-in-cell (PIC) simulations of SNR and HTS shocks (Lembege & Savoini 1992; Schmitz et al. 2002a, 2002b; Scholer et al. 2003; Shimada & Hoshino 2000; Lee et al. 2004, 2005a, 2005b) show that the inclusion of full electron kinetics yields non-stationary solutions: self-reforming shocks, where the reformation occurs on the gyro scales of the incoming ions. The process is controlled by accumulation of reflected ions, where the shock ramp width is on the electron length scale. Reforming solutions for perpendicular shocks were obtained in hybrid simulations by Hellinger et al. (2002), given a suitable tuning of the electron viscosity component.

Detailed studies of particle trajectories have been performed for a range of shock geometries and parameters to investigate the mechanisms that pre-accelerate background ions to mildly relativistic energies. These studies either directly process the trajectories of ions self-consistently evolved in kinetic simulations (e.g., Lee et al. 2005a), or use these simulations to provide the spatio-temporal fields in which the trajectories of test particles are traced (e.g., Zank et al. 1996; Burrows et al. 2010; Yang et al. 2009). A major focus has been on shock drift acceleration and shock surfing acceleration (SSA) mechanisms which respectively involve acceleration as ions drift along the shock front, and (possibly multiple) reflection at the ramp and gyration in the foot region. In reforming shocks, the timing has been found to be crucial in determining the energization of each ion, given that the structure of the ramp varies with the reformation process (Lee et al. 2005a).

SNR plasmas contain significant populations of minority heavy ions (Henry 1986; Ellison et al. 1997, 2001), with relative number densities up to 50% and multiple ion species with ion masses of the order of 10 proton masses. Here, we perform the first fully kinetic self-consistent simulations, which systematically investigate the physical consequences of multispecies ions on the physics of ion pre-acceleration at reforming supercritical shocks. For simplicity, we restrict this first study to two ion species with moderate mass ratios, that is, protons and α-particles. With this choice of a moderate mass

ratio, it is computationally feasible to span the full range of α-particle/proton concentration ratios from 0% to 100%. This will identify any thresholds in the mass concentration ratio at which ion pre-acceleration mechanisms change. Quasi-perpendicular shocks with multiple ion species plasmas have only been treated self-consistently up to $n_\alpha/n_i = 25\%$ (Chapman et al. 2005). Non-self-consistent studies (Yang et al. 2011) have allowed parametric studies of ion injection processes. Both these studies show that the reforming shock can accelerate the minority ion population. The preliminary self-consistent simulation (Chapman et al. 2005) showed that even moderate concentrations of heavy ions can modify the shock reformation spatio-temporal scales.

We perform the first systematic study of perpendicular magnetosonic shocks in plasmas, spanning the full range of relative α-particle densities n_α/n_i from 0% to 100%, where all particle species and fields are modeled self-consistently. The structure of the article is as follows. In Section 2, we describe the numerical methods used in this study and discuss shock geometry and plasma conditions. In Section 3, we introduce our results, in which we (1) demonstrate how the phase space dynamics of the ions change as we increase the α-particle density n_α/n_i, (2) investigate overall ion energization with energy spectra for several n_α/n_i, (3) interpret these with phase space trajectories of individual ions, and finally (4) relate ion energization to power spectral densities of downstream magnetic fields. In Section 4, we summarize our results and present our conclusions. In these simulations, we can identify candidate acceleration mechanisms that occur upon shock injection as well as stochastic diffusion downstream, and we investigate how these depend on the relative ion density n_α/n_i. We do not attempt nor is it feasible within our framework to evolve the diffusion process to obtain final (saturated) energy spectra.

2. SIMULATION DETAILS

We use a 1D3V (where scalar and all three components of vector quantities are functions of one spatial coordinate and time) relativistic electromagnetic PIC code EPOCH. This follows the structure outlined by Lapenta (2012) and has been used to study plasma kinetics across a broad range of applications, including the energization of minority α-particle populations in magnetically confined fusion plasmas (Cook et al. 2010, 2011a, 2011b, 2013). Here, we simulate supercritical, collisionless, perpendicular magnetosonic shocks.

Our simulation setup resembles that of Chapman et al. (2005). Particles are injected through the upstream boundary, where we assume shifted Maxwellian distribution functions satisfying zero charge density and zero current in the upstream region. The upstream magnetic field is set to $\mathbf{B} = B_1\hat{\mathbf{z}}$, and the electric field $\mathbf{E} = E_1\hat{\mathbf{y}}$ is calculated self-consistently, where $\hat{\mathbf{y}}$ and $\hat{\mathbf{z}}$ are unit vectors perpendicular to the plasma inflow. We use the piston method to generate the shock at the lower boundary, and the shock following algorithms to obtain sufficiently long run times (Schmitz et al. 2002b).

To capture both multi-ion species and electron dynamics, we use reduced mass ratios $m_p/m_e = 20$ and $m_\alpha/m_e = 80$ ($m_\alpha/m_p = 4$) and charge ratios $q_p/q_e = -1$ and $q_\alpha/q_p = 2$, corresponding to a plasma consisting of electrons, protons, and α-particles (fully ionized helium). The ratio of plasma frequency ω_{pe} to gyro frequency Ω_e of electrons is $\omega_{pe}/\Omega_e = 20$. In terms of ion dynamics and the overall shock reformation process, numerical simulations in one and two spatial dimensions (retaining all three velocity and field vector components; Lembege & Savoini 1992; Shinohara et al. 2011) and with a reduced mass ratio of protons to electrons (Scholer et al. 2003; Shinohara et al. 2011) are found to produce results similar to simulations in three spatial dimensions and (but not simultaneously) with realistic mass ratios.

Table 1
Normalization Constants

n_α/n_i (%)	V_1 [V_0]	$\mathcal{E}_{p1}$ [$\mathcal{E}_0$]	k_{p1} [k_0]
0	1.00	1.00	1.00
5	0.96	0.92	1.04
10	0.93	0.86	1.08
25	0.86	0.74	1.16
50	0.80	0.64	1.25
75	0.76	0.58	1.31
95	0.74	0.55	1.34
100	0.74	0.55	1.35

The upstream magnetic field is set to $B_1 = 10^{-7}$ T and temperature T_1, corresponding to plasma $\beta = 0.15$ for all species, the values of which are chosen to be those used by Schmitz et al. (2002a, 2002b), Lee et al. (2004, 2005a, 2005b), and Chapman et al. (2005) to allow a comparison of results, while being consistent with estimates of SNR conditions by, e.g., Lucek & Bell (2000). We have electron number density $n_e \approx 4 \times 10^8$ m^{-3} and ion number densities satisfying charge neutrality upstream, $n_e = n_i + 2n_\alpha$, for a given heavy ion density ratio n_α/n_i. We impose an upstream inflow velocity $V_0 = 2 \times 10^7$ m s^{-1} (for an electron–proton plasma) of Mach $M = 8$, with respect to the magnetosonic speed $\sqrt{T_1/m_p + B_1^2/2\mu_0\rho}$. In the shock rest frame, the far upstream (1) and downstream (2) values of shock-normal velocity components are $u_1 = 1.5V_1$ and $u_2 = 0.5V_1$, and the magnetic field $B_2/B_1 = 3$. If we scale these factors to realistic mass ratios m_p/m_e, as in Lee et al. (2004), we obtain $M \approx 100$, $\mathcal{E}_{p1} = 6$ MeV, and $T_1 = 100$ eV.

We simulate a domain of size $L = 20\lambda_{p1}$, where $\lambda_{p1} = m_pV_1/eB_1$ is the upstream gyro radius of protons. Our spatial resolution Δx equals the plasma Debye length $\lambda_D = \sqrt{\epsilon_0 T/\sum_s n_s q_s^2}$, and the time step Δt satisfies the Courant–Friedrichs–Levy condition for electromagnetic waves: $c\Delta t < \Delta x$, so that $\Delta t \approx 3 \times 10^{-6}\tau_{p1}$, where $\tau_{p1} = 2\pi\Omega_{p1}^{-1} = 2\pi m_p/eB_1$ is the upstream gyro period of protons. The ratio $L/\Delta x$ gives ~70,000 cells on our spatial grid, with typically 50 computational particles per species per cell. Our shock following algorithm ensures that the inflow boundary is always at least $5\lambda_{p1}$ upstream of the shock front, which allows ample space for reflected ions in front of the shock and fluctuations in the downstream plasma. All results presented here are in the rest frame of the downstream plasma.

We perform a series of simulations of shocks with the same Mach number for different ratios of ion densities n_α/n_i. Since all other macroscopic quantities are related to each other through the Mach number, we will fix the upstream magnetic field B_1 and allow all other quantities to vary. Specifically, the injection speed V_1, upstream proton kinetic energy $\mathcal{E}_{p1} = m_pV_1^2/2$, upstream gyro radius $\lambda_{p1} = m_pV_1/eB_1$, and corresponding wave number $k_{p1} = 2\pi/\lambda_{p1}$ vary from one simulation to the next. To allow a consistent comparison, where the Mach number is the same for all ion densities, we use normalization constants V_1, $\mathcal{E}_{p1}$, λ_{p1}, and k_{p1} for each relative ion density n_α/n_i. These relate to each other as shown in Table 1, where values for V_1, $\mathcal{E}_{p1}$, and k_{p1} are given relative to reference values V_0, $\mathcal{E}_0$, and k_0 for a pure electron–proton plasma, $n_\alpha/n_i = 0\%$. Normalization constants

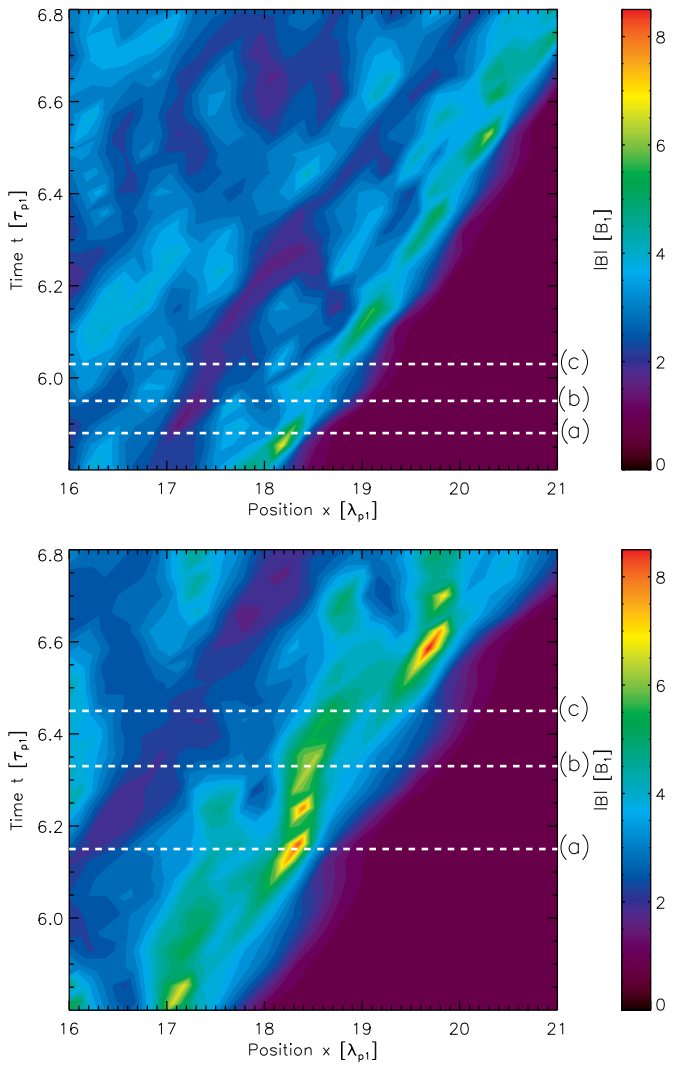

Figure 1. Magnetic field $|B(x,t)|$ (normalized to upstream magnetic field B_1) for $n_\alpha/n_i = 5\%$ (top panel) and $n_\alpha/n_i = 95\%$ (bottom panel) in the rest frame of the downstream plasma, plotted as a function of position x on the horizontal axis (normalized to upstream proton gyro radius λ_{p1}) and time t on the vertical axis (normalized to upstream proton gyro period τ_{p1}). Field strength is indicated by the color bar to the right. The white horizontal dashed lines indicate the times of the snapshots shown in Figures 2 and 3.

(A color version of this figure is available in the online journal.)

for frequency $\Omega_{p1} = eB_1/m_p$ and time $\tau_{p1} = 2\pi/\Omega_{p1}$ do not depend on V_1 and do not vary with n_α/n_i.

3. SIMULATION RESULTS

3.1. Bulk Particle Dynamics and Heating

We first present an overview of how the shock and ion dynamics vary with n_α/n_i. Figure 1 shows the magnetic field as function of position and time in the vicinity of the shock front for both a proton-dominated plasma, $n_\alpha/n_i = 5\%$, and an α-particle-dominated plasma, $n_\alpha/n_i = 95\%$. These plots are in the downstream plasma rest frame and the shock is propagating toward increasing x values. We see that the spatio-temporal scales of the reforming foot and ramp region are governed by the gyro period of the dominant ion species in both cases. We next look in detail at the phase space of ions at the times indicated by the horizontal lines in Figure 1.

Figure 2 shows snapshots at three phases of the shock reformation cycle, at times indicated in the top panel of Figure 1 for $n_\alpha/n_i = 5\%$ when the shock foot extent is (1) at the minimum, (2) growing, and (3) at the maximum. Here, we present snapshots of the u_x versus x and u_y versus x phase space of both ion species, as well as the magnetic field $B_z(x)$ and ion densities n_p, n_α, and $\sum n = n_p + n_\alpha$. The first reflection points of protons and α-particles at the shock are indicated by vertical red and blue lines, respectively. We see that proton dynamics follow the phase of the reformation cycle during which they are incident on the shock front. Protons are quickly thermalized downstream, indicating stochastic acceleration, that is, multiple scattering of ions on the fluctuating electromagnetic fields in the downstream region, leading to diffusive acceleration. α-particles, however, are directly transmitted through the shock front as a mono-energetic beam, following coherent (ordered) trajectories in phase space.

Figure 3 is for a $n_\alpha/n_i = 95\%$ simulation, in the same format as Figure 2, for times indicated in the bottom panel of Figure 1. Here, the roles of the protons and α-particles, and the overall dynamics, are reversed compared to Figure 2: protons now follow coherent trajectories in phase space because all are reflected at the front regardless of the shock reformation phase, whereas α-particles now follow the shock reformation cycle. One key difference between the two simulations is that, when the α-particles are the minority species, they do not gain net energy as they travel through the shock. Energy associated with the bulk motion upstream V_1 translates to gyration downstream with $u_\perp = V_1$. On the other hand, when the protons are in the minority, they gyrate in the front region and gain $u_\perp \rightarrow V_1$. Subsequently, they energize downstream and gain $u_\perp \rightarrow 2V_1$.

Figure 4 shows a sequence of simulations that span the range $n_\alpha/n_i = 5\%$–95%. These are in the same format as Figures 2 and 3, for times when the foot extent is at the minimum. There is a transition at $n_\alpha/n_i \sim 25\%$–50% from protons to α-particles being the species that follows the reformation dynamics of the shock. The majority species appears to be more rapidly thermalized downstream compared to the minority species, for which the motion remains more coherent. The downstream dynamics result in strong density fluctuations which closely correspond to the fluctuations in the downstream magnetic field. In the foot-ramp region of the shock, we find double ramps for intermediate α-particle densities due to density peaks of the respective ion species. The reflection point of protons is consistently found upstream of that of α-particles. Both species always gain at most velocity V_1 in the foot region, consistent with reflection at a stationary shock (Lee et al. 2004), which has been found to be the case in reforming shocks as opposed to non-reforming quasi-perpendicular shocks. Subsequently, in all these cases, the protons when in minority are accelerated to $\sim 2V_1$ in the ramp, while the α-particles when in minority do not gain energy in the foot-ramp region.

3.2. Energetic Particle Dynamics

The key result found in Figures 2–4 is that the majority species controls the shock reformation, while minority species perform coherent dynamics, including acceleration, in the foot-ramp region. We now investigate phase space trajectories and energization of individual ions as they move through the shock and propagate downstream.

We can calculate the work performed on each particle using its full spatio-temporal history $x(t)$ and velocity $\mathbf{u}(t)$, and the fields experienced along the trajectory, $\mathbf{E}(x(t), t)$ and $\mathbf{B}(x(t), t)$.

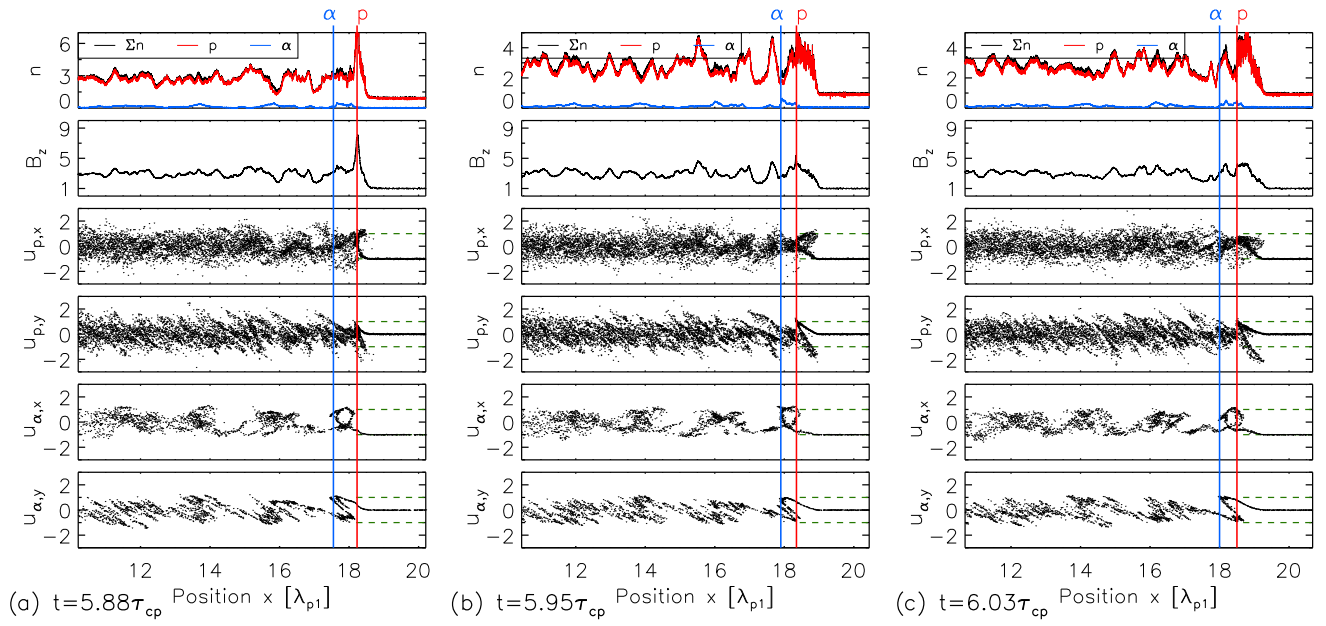

Figure 2. Snapshots in the rest frame of the downstream plasma for $n_\alpha/n_i = 5\%$ at three consecutive times (normalized to the upstream proton gyro period τ_{p1}) when the foot region extent is (a) $t = t_0 = 5.88\tau_{p1}$ (minimum), (b) $t = t_0 + 0.07\tau_{p1}$ (growing), and (c) $t = t_0 + 0.15\tau_{p1}$ (maximum). Panels from top to bottom show quantities plotted against position x (normalized to the upstream proton gyro radius λ_{p1}): (1) total ion, proton, and α-particle number densities ($\sum n = n_p + n_\alpha$, n_p; and n_α; normalized to the upstream electron density n_{e1}), (2) perpendicular magnetic field component B_z (normalized to the upstream magnetic field B_1) and velocities (normalized to the upstream injection velocity V_1 calculated for the respective n_α/n_i; see Section 2), (3) proton velocity parallel to the inflow $u_{p,x}$ and (4) perpendicular to the inflow and magnetic field $u_{p,y}$, (5) α-particle $u_{\alpha,x}$, and (6) $u_{\alpha,y}$. Vertical lines indicate the reflection points near the shock front of protons (colored red online) and α-particles (blue online). Green dashed horizontal lines in velocity panels indicate $u = \pm V_1$.

(A color version of this figure is available in the online journal.)

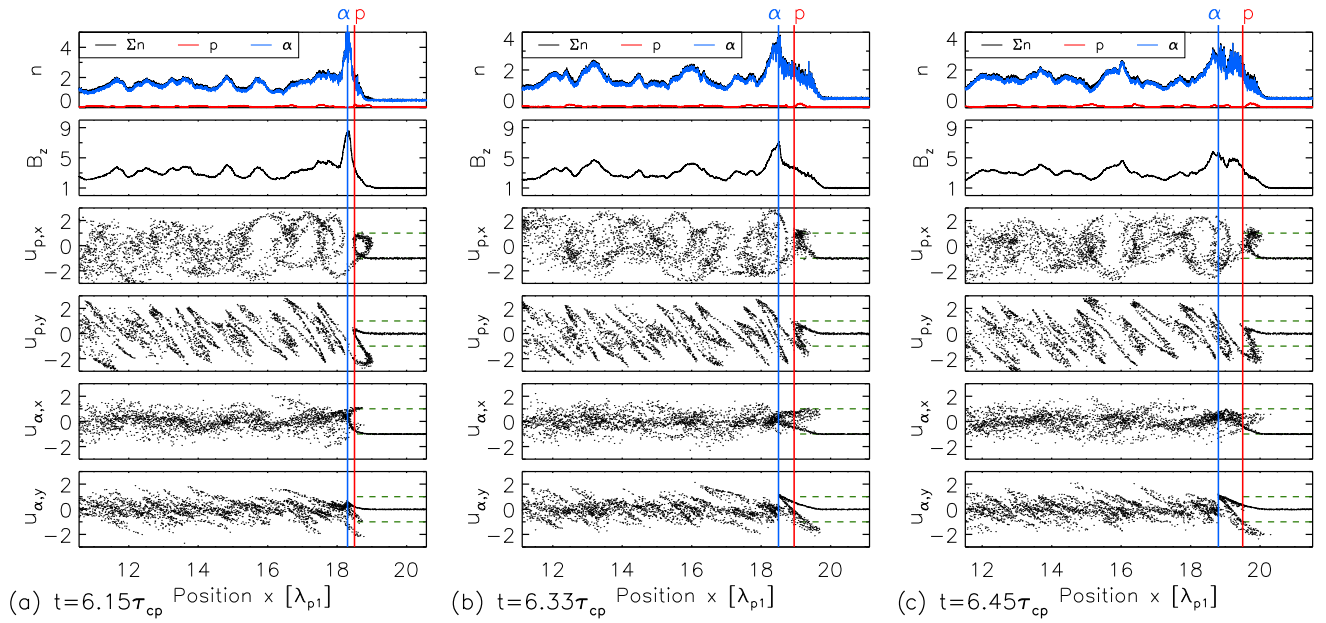

Figure 3. Snapshots in the rest frame of the downstream plasma at three consecutive times for $n_\alpha/n_i = 95\%$ when the extent of the shock foot is (a) $t = t_0 = 6.15\tau_{p1}$ (minimum), (b) $t = t_0 + 0.18\tau_{p1}$ (growing), and (c) $t = t_0 + 0.30\tau_{p1}$ (maximum). Format and normalization are as in Figure 2 for $n_\alpha/n_i = 95\%$ (for normalization, see Section 2).

(A color version of this figure is available in the online journal.)

The particle energy gain between t_0 and t_1 is

$$\Delta\mathcal{E}(t_0, t_1) \equiv q \int_{t_0}^{t_1} \mathbf{u}(t) \cdot \mathbf{E}(t)\, dt. \quad (1)$$

We investigate energization associated with x- and y-motion by plotting the components of the change in energy,

$$\Delta\mathcal{E}_x = q \int u_x E_x dt, \quad \Delta\mathcal{E}_y = q \int u_y E_y dt, \quad (2)$$

where the x-motion is parallel to the inflow and the y-motion is parallel to the induced upstream electric field $\mathbf{E} = E_1\hat{\mathbf{y}}$.

Trajectories of individual ions, drawn from the most energetic component of the population downstream, are shown for $n_\alpha/n_i = 5\%$ in the upper panels of Figure 5, for $n_\alpha/n_i = 95\%$ in Figure 6 and for an intermediate case $n_\alpha/n_i = 25\%$ in Figure 7. Here, we compare spatio-temporal trajectories $x(t)$ plotted over magnetic field strength with energization $\Delta\mathcal{E}(t)$, $\Delta\mathcal{E}_x(t)$, and $\Delta\mathcal{E}_y(t)$.

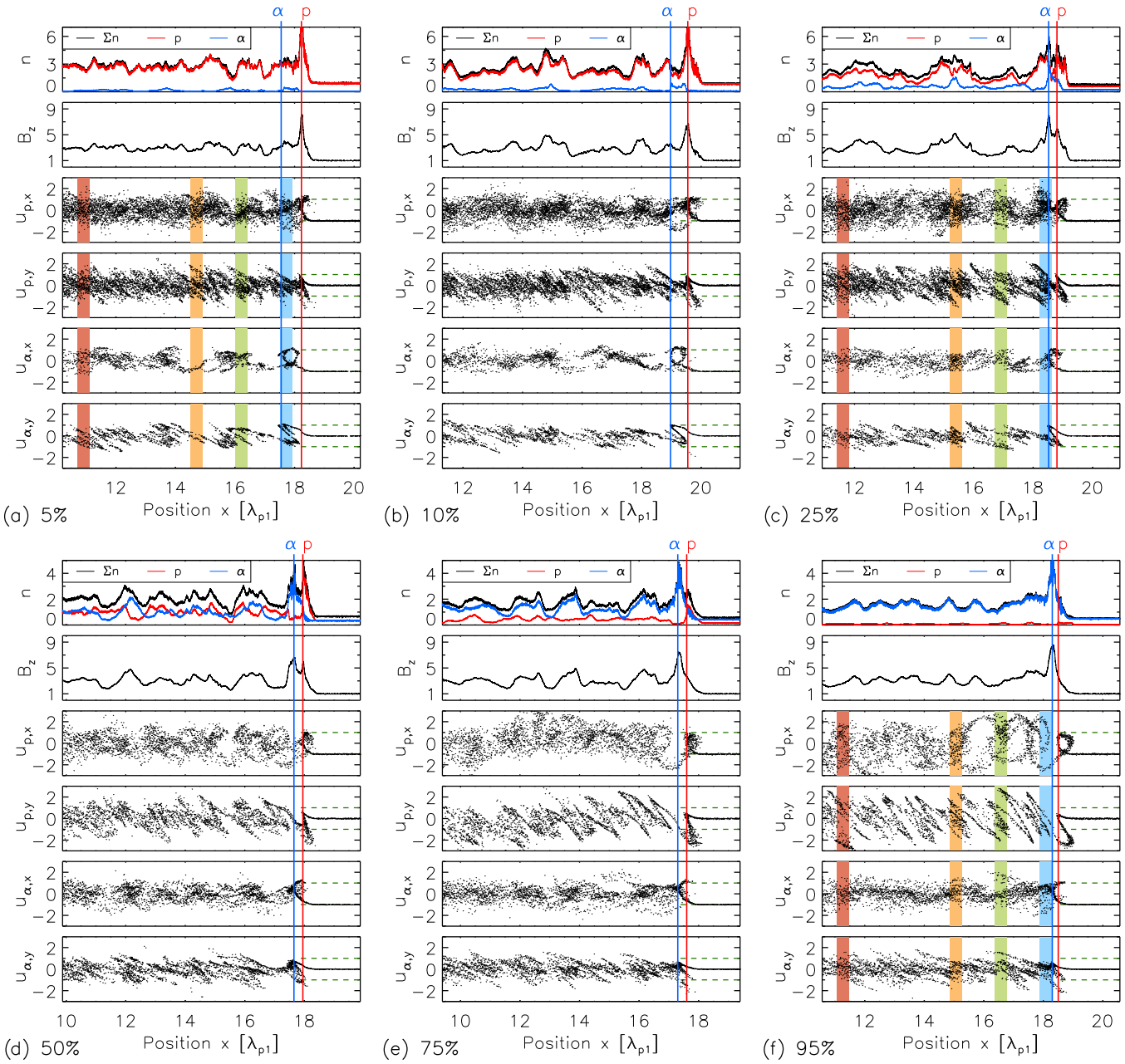

Figure 4. Snapshots in the rest frame of the downstream plasma at times when the foot region extent is at the minimum (corresponding to the left-hand panels of Figures 2 and 3) for (a) $n_\alpha/n_i = 5\%$, (b) 10%, (c) 25%, (d) 50%, (e) 75%, and (f) 95%, in the same format as Figures 2 and 3, with normalization constants calculated for the respective n_α/n_i (see Section 2). Shaded regions in the phase space diagrams indicate centroid positions relative to the shock ramp $\Delta x = -7.5\lambda_{p1}$ (colored red online), $-3.5\lambda_{p1}$ (orange online), $-1.7\lambda_{p1}$ (green online), and $-0.5\lambda_{p1}$ (blue online) of particle ensembles for which energy spectra presented in Section 3.2 are calculated.

(A color version of this figure is available in the online journal.)

In the lower panels of Figures 5–7, we plot total energy spectra $f_\mathcal{E}(\mathcal{E}_p)$ and $f_\mathcal{E}(\mathcal{E}_\alpha)$, normalized to unity $\int \mathcal{E}_{p1} f_\mathcal{E}(\mathcal{E}_p/\mathcal{E}_{p1}) d\mathcal{E}_p = \int \mathcal{E}_{p1} f_\mathcal{E}(\mathcal{E}_\alpha/\mathcal{E}_{p1}) d\mathcal{E}_\alpha = 1$, where $\mathcal{E}_i = \mathcal{E}_{i1} + \Delta\mathcal{E}(t)$. Spectra are calculated from ensembles of 700,000 particles, initially selected while upstream, then traced as they travel through the shock front. Spectra are calculated once they are upstream, at time $\Delta\tau = -0.7\tau_{p1}$, relative to when the ensembles arrive at the shock front (where $\tau_{p1} = 2\pi\Omega_{p1}^{-1}$ is the upstream proton gyro period), and at four times when they are downstream $\Delta\tau = 0.1\tau_{p1}$, $0.7\tau_{p1}$, $1.2\tau_{p1}$, and $2.4\tau_{p1}$. At the latter time, the ions have typically completed 10 (protons) and 5 (α-particles) gyro orbits. Energy is normalized to proton injection energy $\mathcal{E}_{p1}$ of the respective ion densities n_α/n_i which, from the arguments given in Section 2, decrease with increasing n_α/n_i. The centroid positions of the particle ensembles at times $\Delta\tau$ are indicated by shaded regions in Figure 4.

Figure 5 shows two proton trajectories (A and B) and one α-particle trajectory (C) for a proton-dominated plasma, $n_\alpha/n_i = 5\%$. The final particle energies are indicated by arrows in the energy spectra in the same figure. The most prominent difference between protons A and B is that proton A is accelerated at the shock front, whereas B is directly transmitted without significant acceleration. Stochastic acceleration downstream remains equally efficient for the two, regardless of their shock

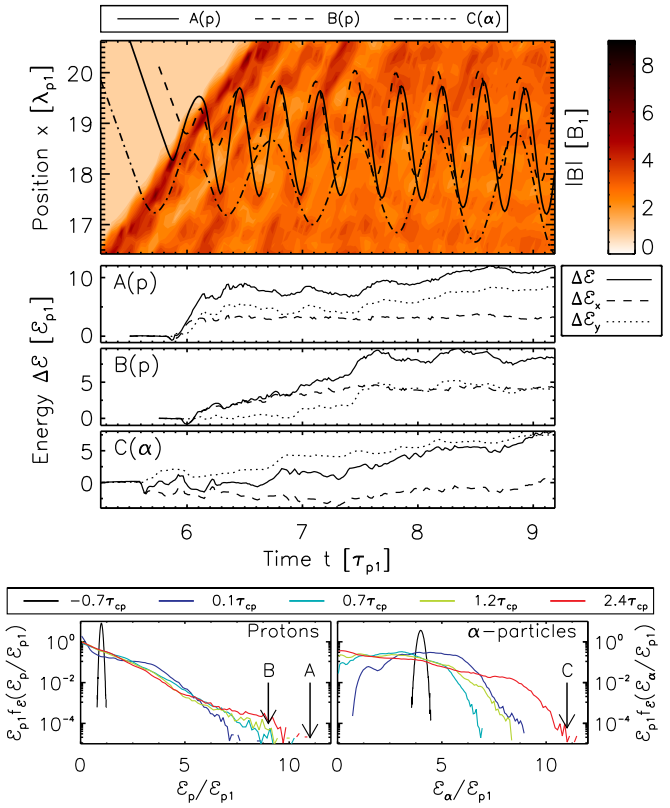

Figure 5. Individual trajectories of protons (A, B) and an α-particle (C) in the rest frame of the downstream plasma for a simulation with $n_\alpha/n_i = 5\%$, plotted as functions of time (normalized to upstream gyro period τ_{p1} of protons). Upper panel: particle position $x(t)$ (normalized to upstream gyro radius of protons λ_{p1}) plotted over the spatio-temporal evolution of magnetic field $|B(x,t)|$ (normalized to upstream magnetic field B_1). The lower three panels plot the change in kinetic energies: in total, $\Delta\mathcal{E}(t)$; of x-motion, $\Delta\mathcal{E}_x(t)$; and of y-motion, $\Delta\mathcal{E}_y(t)$, normalized to proton injection energy $\mathcal{E}_{p1}$ calculated for the given n_α/n_i (see Section 2). Bottom panels: energy spectra of protons (left) and α-particles (right). Energy spectra are calculated at five consecutive times $\Delta\tau$, one before crossing the shock front, $\Delta\tau = -0.7\tau_{p1}$, and four after $\Delta\tau = 0.1\tau_{p1}$, $0.7\tau_{p1}$, $1.2\tau_{p1}$, and $2.4\tau_{p1}$, with corresponding particle ensemble centroid locations as indicated by shaded regions in Figure 4. The final energies of trajectories A, B, and C are indicated by arrows.

(A color version of this figure is available in the online journal.)

front energization. The α-particle (C), on the other hand, gains no energy at the front and is only accelerated further downstream. Energization due to y-motion may have saturated for B, but not for A and C. The energy spectra support this interpretation, because the high-energy tails continue to evolve at late times in these simulations. The knee (or cutoff) in the α-particle energy spectra further indicates that thermalization is not complete.

Figure 6 shows one proton (A) and one α-particle (B) trajectory in an α-particle dominated plasma, $n_\alpha/n_i = 95\%$, where the final energies of A and B are indicated in the energy spectra. The time history of α-particle B, which is now the majority species, closely resembles that of proton A in Figure 5, where protons are the majority species. In both cases, energy spectra $f_\mathcal{E}(\mathcal{E})$ of the majority species have formed energetic tails while the minority species have not.

Figure 7 shows an intermediate case where $n_\alpha/n_i = 25\%$. We find a much larger variation in phase space trajectories in this simulation compared to those for $n_\alpha/n_i = 5\%$ and 95%, suggesting that a broader variety of energization paths are available to both species. We also see more extended high-energy tails for both ion species in the energy spectra, suggesting

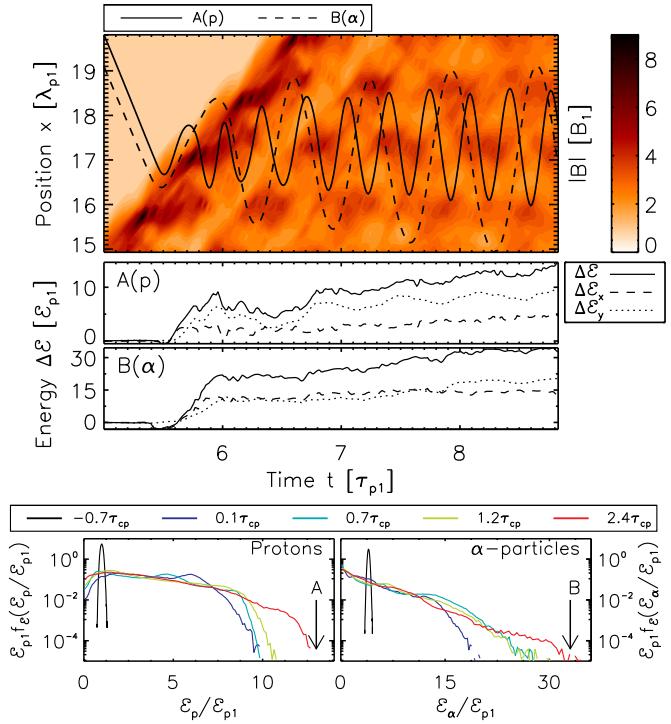

Figure 6. Individual trajectories of a proton (A) and α-particle (B) in the rest frame of the downstream plasma for $n_\alpha/n_i = 95\%$, together with ion energy spectra, in the same format as Figure 5.

(A color version of this figure is available in the online journal.)

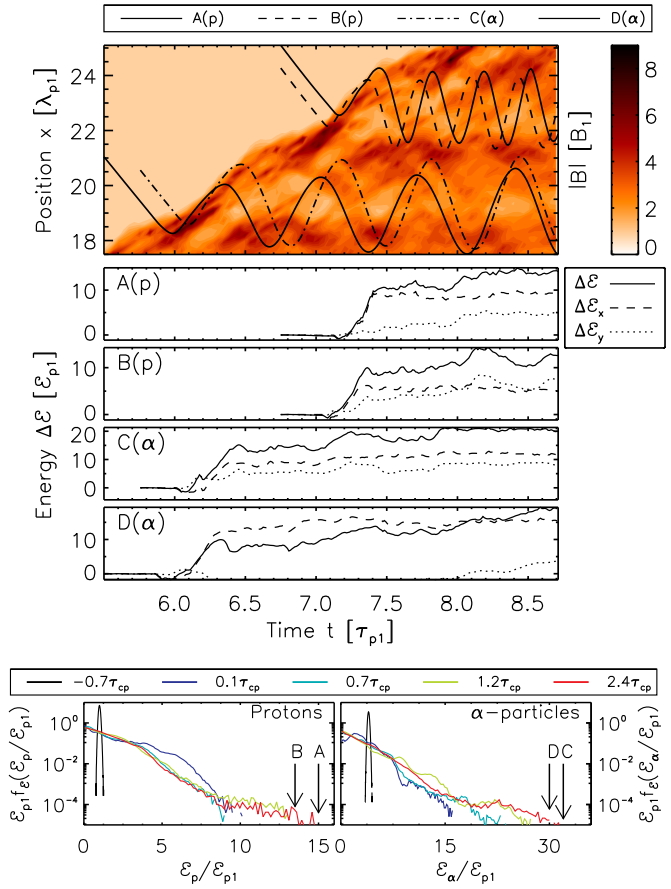

Figure 7. Individual trajectories of protons (A and B) and α-particles (C and D) in the rest frame of the downstream plasma for $n_\alpha/n_i = 25\%$, together with ion energy spectra, in the same format as Figures 5 and 6.

(A color version of this figure is available in the online journal.)

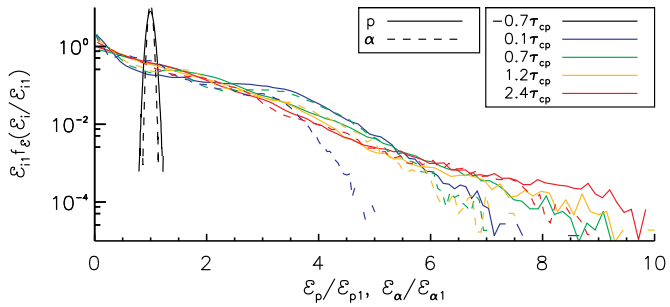

Figure 8. Energy spectra of the majority ion species in the rest frame of the downstream plasma, i.e., protons for $n_\alpha/n_i = 5\%$ and α-particles for $n_\alpha/n_i = 95\%$. Energy spectra are calculated at five consecutive times $\Delta\tau$, one before crossing the shock front, $\Delta\tau = -0.7\tau_{p1}$, and four after $\Delta\tau = 0.1\tau_{p1}$, $0.7\tau_{p1}$, $1.2\tau_{p1}$, and $2.4\tau_{p1}$, with corresponding particle ensemble centroid locations as indicated by the shaded regions in Figure 4. Spectra of both species are normalized to each respective upstream injection kinetic energy, i.e., $\mathcal{E}_p/\mathcal{E}_{p1}$ and $\mathcal{E}_\alpha/\mathcal{E}_{\alpha 1}$, satisfying $\int \mathcal{E}_1 f_\mathcal{E}(\mathcal{E}/\mathcal{E}_i)d\mathcal{E}_i = 1$ for both ion species.

(A color version of this figure is available in the online journal.)

that these intermediate cases are potentially more efficient at particle acceleration.

In Figure 8, we test the idea that the majority species energization follows a simple parametric scaling. The energy spectra of two simulations, here $n_\alpha/n_i = 5\%$ and 95%, are normalized to the upstream injection kinetic energy of the majority species, i.e., $\mathcal{E}_{\alpha 1} f_\mathcal{E}(\mathcal{E}_\alpha/\mathcal{E}_{\alpha 1})$ and $\mathcal{E}_{p1} f_\mathcal{E}(\mathcal{E}_p/\mathcal{E}_{p1})$. These spectra then collapse over each other except at the highest energies where statistics are poor. The energy spectra of the majority species, when scaled to each respective ion species injection energy, $\mathcal{E}_{p1}$ and $\mathcal{E}_{\alpha 1}$, overlap well, indicating that shock energization scales with the injection energy of the ion species. This is not the case for the minority ion species, where protons are found to gain more energy relative to their injection energy than α-particles. In this case, at least for the acceleration in the foot ramp, the scaling is identifiable from Figures 2–4, where minority protons gain $2V_1$.

3.3. Wave Energy

In Figures 2–4, the beginning of thermalization can be seen in the downstream region when ions can scatter off magnetic field fluctuations. While these simulations cannot run for a sufficient length of time to follow the full thermalization and stochastic heating of the ions, we can identify the nature of the downstream fluctuations that contribute to this stochastic process.

We analyze power spectra $P(k, \omega)$ of the magnetic field $|B(x, t)|$ as functions of wave number k and frequencies ω in the rest frame of the downstream plasma during a finite time $[t_0, t_0 + T_D]$ and within a finite region $[x_0, x_0 + L_D]$ using Welch's method (Welch 1967). We integrate the power spectra $P(k, \omega)$ for $\omega > 0$ over k to obtain the frequency spectrum $P(\omega)$. The discrete nature of the input signal $B(x, t)$, reflecting the finite diagnostic output time interval $\Delta t_D = \tau_{p1}/20$ and total sampling time $T_D = 1.6\tau_{p1}$, places upper and lower limits on the frequency domain, $\omega \in [2\pi/T_D, 2\pi/\Delta t_D] = [0.6\Omega_{p1}, 20\Omega_{p1}]$.

Figure 9 shows frequency spectra $P(\omega)$ for simulations with ion densities ranging from $n_\alpha/n_i = 0\%$ to 100%. The spectra have multiple peaks at harmonics of the downstream ion gyro frequencies of the protons and α-particles. The gyro frequencies in the magnetic field far downstream (2) $\langle B_2 \rangle = 3B_1$ are indicated in the plot for protons Ω_{p2} and α-particles $\Omega_{\alpha 2}$. As the fraction of α-particles is increased, the total power increases. As Ω_{p2} harmonics are coincident with $\Omega_{\alpha 2}$, these are always present. We can see that there is a systematic increase in power at the harmonics of $\Omega_{\alpha 2}$ as the relative ion density n_α/n_i is increased.

There appear to be points of contact between the simulation results encapsulated in Figure 9 and the physics of edge-localized minority energetic ions in magnetic confinement fusion plasmas. Specifically, suprathermal emission at multiple sequential ion cyclotron harmonics is observed in fusion plasmas containing a minority ring-beam population of energetic ions. Perhaps most notably, this ion cyclotron emission (ICE) was driven by minority energetic (3.5 MeV) particles born in fusion reactions between thermal (10 keV to 20 keV) deuterons and tritons confined in the Joint European Torus (JET) and TFTR experiments. Here, energetic minority ring-beam populations arose naturally at the outer midplane edge (Cottrell et al. 1993; Dendy et al. 1995) because of drift orbit effects. ICE was detected using heating antennas, designed to launch the fast Alfvén wave, as receivers on JET. Analytical theory, contemporary with the JET and TFTR observations, suggested that the excitation mechanism for ICE is the magnetoacoustic cyclotron instability (MCI), driven by a set of centrally born fusion products, lying just inside the trapped–passing boundary in velocity space, whose drift orbits make large radial excursions to the outer midplane edge (Dendy et al. 1994; Cauffman et al. 1995). Recent first-principle fully nonlinear PIC (Cook et al. 2013) and hybrid (Carbajal et al. 2014) simulations of the MCI confirm that the dominant excited modes are fast Alfvén. That is, fluctuations in density and magnetic field strength are approximately in phase, as is also the case in the downstream turbulence giving rise to Figure 9. Phenomenology similar to ICE in fusion experiments has been observed in terrestrial magnetospheric plasmas (McClements & Dendy 1993; Dendy & McClements 1993). The possibility of related effects at SNR shocks was noted by McClements et al. (1996). For example, first-principle direct numerical simulations show that waves excited in this range of frequency and wavelength are capable of pre-accelerating electrons in SNR environments (Dieckmann et al. 2000; Schmitz et al. 2002a, 2002b).

There is a spectral peak $\Omega_{\mathrm{LH}\alpha}$ for the lowest α-particle concentrations $n_\alpha/n_i \leqslant 5\%$. While waves in this frequency range are known to be excited by ring-beam (and other) minority energetic α-particle populations (Cook et al. 2010, 2011a, 2011b), this peak is more likely to be the third cyclotron harmonic of the protons, which is nearly degenerate with the lower hybrid frequency of α-particles. No noticeable peak is found at the lower hybrid frequency of protons in any proton-dominated simulation, and no peak at the lower hybrid frequency of α-particles is found in simulations where α-particles dominate.

Finally, in Figure 10, we plot a representative power spectrum $P(k, \omega)$ against wave number and frequency for a simulation where $n_\alpha/n_i = 50\%$. The full k, ω-spectrum is broadband but has the most energy within the phase speeds $\omega/k = (0.6\text{–}1)V_1$. The value $0.6V_1$ corresponds to the magnetosonic wave speed in the downstream regions, assuming average downstream (2) macroscopic values for the magnetic field $\langle B_2 \rangle \approx 3B_1$, mass density $\langle \rho_2 \rangle \approx 2.5\rho_1$, and temperature $\langle T_2 \rangle \approx 50T_1$ with respect to upstream quantities (1). However, we can also interpret these fluctuations as a non-propagating mode that arises as a consequence of the density fluctuations downstream, which in turn directly relate to the downstream ion dynamics. We have seen that magnetic field B_2 and ion density n_2 fluctuations

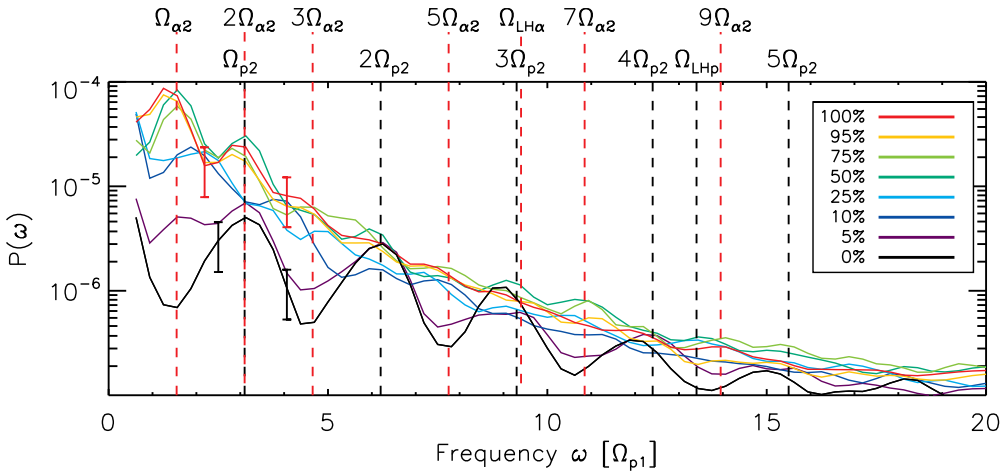

Figure 9. Power spectra of temporal fluctuations in the magnetic field $|B(x,t)|$, downstream of the shock front, in the plasma rest frame. Spectra are shown for $n_\alpha/n_i = 0\%$, 5%, 10%, 25%, 50%, 75%, 95%, and 100%. B is normalized to the ratio of the injection kinetic energy of protons $\mathcal{E}_{p1}$ to the upstream gyro frequency Ω_{p1}. We plot $P(\omega)$ vs. frequency ω/Ω_{p1} for $\omega > 0$. Gyro frequencies of protons Ω_{p2} and α-particles $\Omega_{\alpha 2}$ (and higher harmonics of these) in a downstream magnetic field $B_2 = 3B_1$ are indicated by vertical dashed lines (red for α-particles, black for protons). The expected values of lower hybrid frequencies of an electron–proton plasma $\Omega_{\mathrm{LH}p}$ and electron–α-particle plasma $\Omega_{\mathrm{LH}\alpha}$ are also indicated.

(A color version of this figure is available in the online journal.)

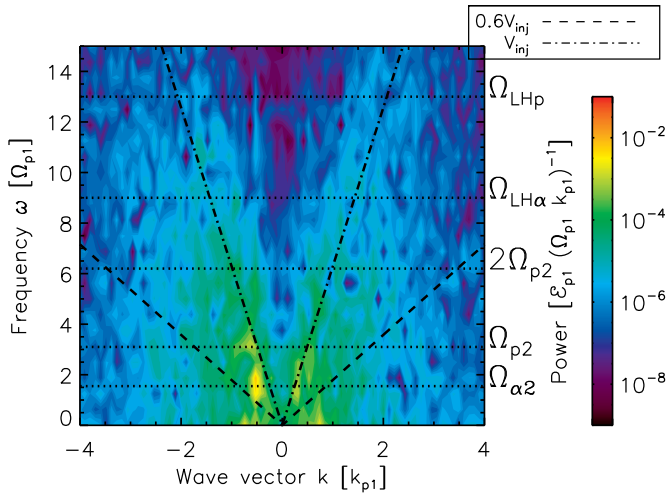

Figure 10. Power spectrum of spatio-temporal fluctuations in the magnetic field $|B(x,t)|$ of the downstream region for $n_\alpha/n_i = 50\%$, in the rest frame of the plasma. B is normalized to the ratio of the injection kinetic energy of protons $\mathcal{E}_{p1}$ to the upstream gyro frequency Ω_{p1}, and wave number to the upstream gyro radius $k_{p1} = 2\pi\lambda_{p1}^{-1}$. We plot $P(k,\omega)$ vs. frequency ω/Ω_{p1} and wave number k/k_{p1} for $\omega > 0$. Gyro frequencies in the downstream magnetic field $\langle B_2\rangle = 3B_1$, $\Omega_{\alpha 2}$, and Ω_{p2} (and their higher harmonics), as well as lower hybrid oscillation frequencies $\Omega_{\mathrm{LH}\alpha}$ and $\Omega_{\mathrm{LH}p}$ are indicated by horizontal (dotted) lines. Lines for $\omega/k = \pm u$ are plotted for $u = 0.6V_1$ (dash) and $u = V_1$ (dash–dotted).

(A color version of this figure is available in the online journal.)

strongly correlate downstream. The spatial scale is then that of the downstream gyration $u_\perp/\Omega$, and the temporal scale is that of the downstream gyro period $1/\Omega$. Thus, $\omega/k \equiv u_\perp$ and the value $u_\perp$ ranges from V_1 to $\sim 0.5V_1$ for directly transmitted and accelerated ions.

4. CONCLUSIONS

In this paper, we present the first fully self-consistent PIC simulations that systematically span the range of relative heavy ion densities $n_\alpha/n_i = 0\%$–100%. We find that spatio-temporal scales of the foot-ramp region and downstream fluctuations depend on n_α/n_i. In a shock dominated by one ion species, the shock dynamics are controlled by the majority species and the energy gain of the majority species scales with the inflow energy for a given Mach number. Thermalization of the majority species downstream is rapid although not complete. Energization occurs both by reflection of subsets of ions at the foot ramp and by stochastic motion in turbulence generated downstream. The interaction with the foot ramp may be characterized as a single coherent gyration; we do not see multiple interactions with the foot-ramp region as are suggested to occur in, for example, SSA. The minority species dynamics remain coherent through the shock. On encountering the foot ramp, the upstream bulk speed V_1 is translated to gyrational motion with perpendicular velocity $u_\perp \rightarrow V_1$. The α-particles do not gain net energy, whereas the protons ultimately gain up to $u_\perp \rightarrow 2V_1$. For intermediate cases of n_α/n_i, there are several paths to energization, and net energization of both species is enhanced compared to the cases where one species is the majority. Fluctuations downstream embody dominant density structures that are in turn generated by the ion dynamics. These can act to thermalize the ions. Our results are consistent with the findings of Chapman et al. (2005) and Yang et al. (2011).

Astrophysical plasmas typically contain several minority species with intermediate relative number densities. Our simulations show that ion energization, for intermediate heavy ion densities, gives rise to extended high-energy tails in the energy spectra. This suggests that real astrophysical shocks have favorable conditions for accelerating ions to suprathermal energies.

Oblique wave modes and waves propagating perpendicular to the direction of inflow are not captured by the current simulations, due to the exact perpendicular geometry of the shock. We are thus unable to model wave–particle interactions due to such wave modes and energy transport perpendicular to the inflow. However, our simulations are sufficient to capture the essential shock reformation process.

The work was supported in part by the Research Council of Norway, the UK Engineering and Physics Sciences Research Council under grant EP/G003955, and by the European Communities under the contract of association between Euratom

and CCFE. The views and opinions expressed herein do not necessarily represent those of the European Communities. The EPOCH code used in this research was developed under UK Engineering and Physics Sciences Research Council grants EP/G054940/1, EP/G055165/1, and EP/G056803/1. We thank Professors H. L. Pécseli and J. K. Trulsen for their interest and many valuable discussions on the subject.

REFERENCES

Bell, A. B. 1978, MNRAS, 182, 147
Blandford, R. D., & Ostriker, J. P. 1978, ApJL, 221, L29
Burrows, R. H., Zank, G. P., Webb, G. M., Burlaga, L. F., & Ness, N. F. 2010, ApJ, 715, 1109
Carbajal, L., Dendy, R. O., Chapman, S. C., & Cook, J. W. S. 2014, PhPl, 21, 012106
Cauffman, S., Majeski, R., McClements, K., & Dendy, R. 1995, NucFu, 35, 1597
Chapman, S. C., Lee, R. E., & Dendy, R. O. 2005, SSRv, 121, 5
Cook, J. W. S., Chapman, S. C., & Dendy, R. O. 2010, PhRvL, 105, 255003
Cook, J. W. S., Chapman, S. C., Dendy, R. O., & Brady, C. S. 2011a, PPCF, 53, 065006
Cook, J. W. S., Dendy, R. O., & Chapman, S. C. 2011b, PPCF, 53, 074019
Cook, J. W. S., Dendy, R. O., & Chapman, S. C. 2013, PPCF, 55, 065003
Cottrell, G., Bhatnagar, V., Costa, O. D., et al. 1993, NucFu, 33, 1365
Dendy, R., McClements, K., Lashmore-Davies, C., et al. 1995, NucFu, 35, 1733
Dendy, R. O., Lashmore-Davies, C. N., McClements, K. G., & Cottrell, G. A. 1994, PhPl, 1, 1918
Dendy, R. O., & McClements, K. G. 1993, JGR, 98, 15531
Dieckmann, M. E., Eliasson, B., Shukla, P. K., Sircombe, N. J., & Dendy, R. O. 2006, PPCF, 48, B303
Dieckmann, M. E., McClements, K. G., Chapman, S. C., Dendy, R. O., & Drury, L. O. 2000, A&A, 356, 377
Ellison, D. C., Drury, L. O., & Meyer, J.-P. 1997, ApJ, 487, 197
Ellison, D. C., Slane, P., & Gaensler, B. M. 2001, ApJ, 563, 191
Enomoto, R., Tanimori, T., Naito, T., et al. 2002, Natur, 416, 423
Fermi, E. 1949, PhRv, 75, 1169
Hellinger, P., Travnicek, P., & Matsumoto, H. 2002, GeoRL, 29, 2234
Henry, R. C. B. 1986, PASP, 98, 1044
Kirk, J. G., & Dendy, R. O. 2001, JPhG, 27, 1589
Koyama, K., Petre, R., & Gotthelf, E. V. 1995, Natur, 378, 225
Lapenta, G. 2012, JCoPh, 231, 795
Lee, R. E., Chapman, S. C., & Dendy, R. O. 2004, ApJ, 604, 187
Lee, R. E., Chapman, S. C., & Dendy, R. O. 2005a, PhPl, 12, 012901
Lee, R. E., Chapman, S. C., & Dendy, R. O. 2005b, AnGeo, 23, 643
Lembege, B., & Savoini, P. 1992, PhFlB, 4, 3533
Lucek, S. G., & Bell, A. R. 2000, MNRAS, 314, 65
McClements, K., Dieckmann, M. E., Ynnerman, A., Chapman, S., & Dendy, R. 2001, PhRvL, 87, 255002
McClements, K. G., & Dendy, R. O. 1993, JGR, 98, 11689
McClements, K. G., Dendy, R. O., Drury, L. O., & Duffy, P. 1996, MNRAS, 280, 219
Schmitz, H., Chapman, S. C., & Dendy, R. O. 2002a, ApJ, 579, 327
Schmitz, H., Chapman, S. C., & Dendy, R. O. 2002b, ApJ, 570, 637
Scholer, M., Shinohara, I., & Matsukiyo, S. 2003, JGR, 108, 1014
Shimada, N., & Hoshino, M. 2000, ApJL, 543, L67
Shinohara, I., Fujimoto, M., Takaki, R., & Inari, T. 2011, ITPS, 39, 1173
Welch, P. 1967, IEEE Trans. Audio Electroacoust., 15, 70
Yang, Z. W., Lembege, B., & Lu, Q. M. 2011, JGR, 116, A10202
Yang, Z. W., Lu, Q. M., Lembege, B., & Wang, S. 2009, JGR, 114, A03111
Zank, G. P., Pauls, H. L., Cairns, I. H., & Webb, G. M. 1996, JGRA, 101, 457